The Astrophysical Journal, 599:1333–1343, 2003 December 20

IONIZING PHOTON EMISSION RATES FROM O- AND EARLY B-TYPE STARS AND CLUSTERS

Amiel Sternberg
School of Physics and Astronomy and the Wise Observatory, The Beverly and Raymond Sackler Faculty of Exact Sciences, Tel Aviv University, Tel Aviv 69978, Israel

and

Tadziu L. Hoffmann and A. W. A. Pauldrach
Institute for Astronomy and Astrophysics of the Munich University, Scheinerstraße 1, D-81679 Munich, Germany
Received 2003 June 17; accepted 2003 August 29

ABSTRACT

We present new computations of the ionizing spectral energy distributions (SEDs), and Lyman continuum (Lyc) and He I continuum photon emission rates, for hot O-type and early B-type stars. We consider solar-metallicity stars, with effective temperatures ranging from 25,000 to 55,000 K and surface gravities (cm s^{-2}) log g ranging from 3 to 4, covering the full range of spectral types and luminosity classes for hot stars. We use our updated (*WM-basic*) code to construct radiation-driven wind atmosphere models for hot stars. Our models include the coupled effects of hydrodynamics and non-LTE radiative transfer in spherically outflowing winds, including the detailed effects of metal line blocking and line blanketing on the radiative transfer and energy balance. Our grid of model atmospheres is available on the World Wide Web. We incorporate our hot-star models into our population synthesis code (STARS), and we compute the time-dependent SEDs and resulting Lyc and He I emission rates for evolving star clusters. We present results for continuous and impulsive star formation for a range of assumed stellar initial mass functions.

Subject headings: H II regions — stars: atmospheres — stars: early-type — stars: fundamental parameters

1. INTRODUCTION

Massive hot stars inject large amounts of energy and entropy into the interstellar medium of galaxies via jets, winds, radiation, and supernova explosions. The production rates of Lyman continuum photons (Lyc; $h\nu > 13.6$ eV), and of helium continuum photons (He I; $h\nu > 24.6$ eV), are particularly important and fundamental parameters of O-type and early B-type stars (Mihalas 1967; Panagia 1973; Vacca, Garmany, & Shull 1996; Schaerer & de Koter 1997; Lanz & Hubeny 2003). The ionizing radiation produces H II regions around the hot stars, and the photon fluxes determine the intensities of hydrogen and helium recombination lines, collisionally excited metal emission lines, and free-free continuum fluxes from the photoionized gas. Massive stars often form in groups or clusters, as in Galactic OB associations (McKee & Williams 1997) or in more massive super–star clusters observed in galaxy nuclei and starburst galaxies (Whitmore et al. 1999; Maoz et al. 2001). Such objects can contain thousands of individual OB stars within small volumes, and the associated nebular emissions are detectable to large redshifts (e.g., Shapley et al. 2003).

In this paper, we present new computations of the Lyc and He I photon emission rates for hot stars, using our updated radiation-driven wind atmosphere models for O-type and early B-type stars (Pauldrach, Hoffmann, & Lennon 2001). Our models include the coupled effects of hydrodynamics and non-LTE (NLTE) radiative transfer, in spherically outflowing radiation-driven winds, including the detailed effects of line blocking and line blanketing on the radiative transfer and energy balance. In this paper we focus on solar-metallicity systems, and we present results for a model grid spanning a wide range of stellar effective temperatures and surface gravities, covering the full range of stellar types from dwarfs to supergiants. Low-metallicity systems such as those occurring in dwarf galaxies (e.g., Lee, Grebel, & Hodge 2003) or in the early universe (Tumlinson & Shull 2000; Schaerer 2003) will be considered elsewhere.

We use our stellar atmosphere grid, in combination with evolutionary models, to carry out "population synthesis" computations (Bruzual & Charlot 1993; Leitherer & Heckman 1995; Sternberg 1998; Leitherer et al. 1999) of the time-dependent spectral energy distributions (SEDs), and time-dependent Lyc and He I photon emission rates, for evolving star clusters. We present results for the two limiting cases of "continuous" and "impulsive" star formation, for a range of assumed stellar initial mass functions. Our cluster synthesis computations may be used together with observational continuum and emission-line data to infer star formation rates and histories in Galactic and extragalactic star-forming regions.

In § 2, we summarize the basic ingredients of our stellar atmosphere models. In § 3, we fix the various empirically based input parameters, including the stellar radii, surface gravities, effective temperatures, terminal wind velocities, and mass-loss rates. In § 4, we discuss the model atmospheres, present the Lyc and He I photon emission rates as functions of the stellar parameters, and compare our results to previous computations presented in the literature. In § 5, we present the results of our population synthesis computations for cluster SEDs and associated Lyc and He I photon emission rates.

2. MODEL ATMOSPHERES

We use our NLTE wind-driven stellar atmosphere code (*WM-basic*) to compute hot-star spectral energy distributions for a wide range of stellar input parameters. Details of this code, and the modelling methods, are presented in Pauldrach et al. (2001). Here we provide a brief description.

The *WM-basic* code iteratively solves the coupled equations of hydrodynamics, energy balance, and NLTE radiative transfer, for spherically symmetric radiatively driven steady state winds expanding off the photospheres of hot stars. The hydrodynamic equations are solved for pre-specified values of the stellar effective temperature $T_{\rm eff}$, surface gravity log g, photospheric radius R_*, and metallicity Z. Given the solutions to the hydrodynamic density and velocity structures, the local NLTE occupation numbers for approximately 5000 atomic levels are determined by solving the microscopic population rate equations, including radiative and collisional excitation and de-excitation processes, in several million line transitions of elements from H to Zn. The strong "line blocking" attenuation of the ultraviolet (UV) radiation fluxes (both ionizing and nonionizing) by the numerous spectral lines in the UV spectral range is properly included in the radiative transfer, with significant influence on the NLTE level populations. The "line blanketing" heating of the photosphere as a consequence of this blocking of radiation is accounted for in the temperature structure, which is determined by solving the energy balance equation. The radiation field, opacities, emissivities, and occupation numbers at all depths in the wind are determined consistently via a detailed computation of the radiation transfer in the observer's frame, and an explicit solution of the rate equations incorporating all significant microscopic processes. The solution to the radiative transfer equation finally also yields the escaping radiation field in the form of the SED and synthetic stellar spectrum.

The steady state flow, in both the supersonic and subsonic regions, is controlled by the radiative acceleration provided by the combined effects of continuum and line absorption. In the computations we present here, we adjust the absorption line "force multiplier" parameters, k, α, and δ (Castor, Abbott, & Klein 1975; Abbott 1982), such that the resulting hydrodynamics mass-loss rates, $\dot{M}$, and terminal flow velocities, v_∞, are consistent with observations (see § 3).

Our "realistic" NLTE radiation-driven wind atmosphere models provide excellent matches to directly observable far-UV stellar SEDs longward of the Lyman limit (e.g., Pauldrach et al. 2001). Crucially, the computed far-UV spectra depend on the detailed NLTE solutions throughout the winds, which, in turn, depend primarily on the ionization states of species with ionization potentials *shortward* of the Lyman limit. Thus, the excellent match to observed far-UV SEDs is direct evidence that the ionizing continua are computed accurately in our models, and that additional physical processes, such as gas clumping, have only minor effects. Further supporting evidence for the accuracy of our models comes from successful fits to the relative intensities of (infrared) emission lines observed in Galactic H II regions, in nebular photoionization calculations that explicitly incorporate our hot-star models (Giveon et al. 2002).

3. STELLAR PARAMETERS

We have constructed a detailed grid of OB star model atmospheres for all luminosity classes, from main-sequence dwarfs to supergiants. We adopt solar metals abundances as compiled by Grevesse & Sauval (1998). The input parameters for each model are the effective temperature, surface gravity, and stellar radius,[1] as well as the terminal wind velocity, v_∞, and mass-loss rate, $\dot{M}$.

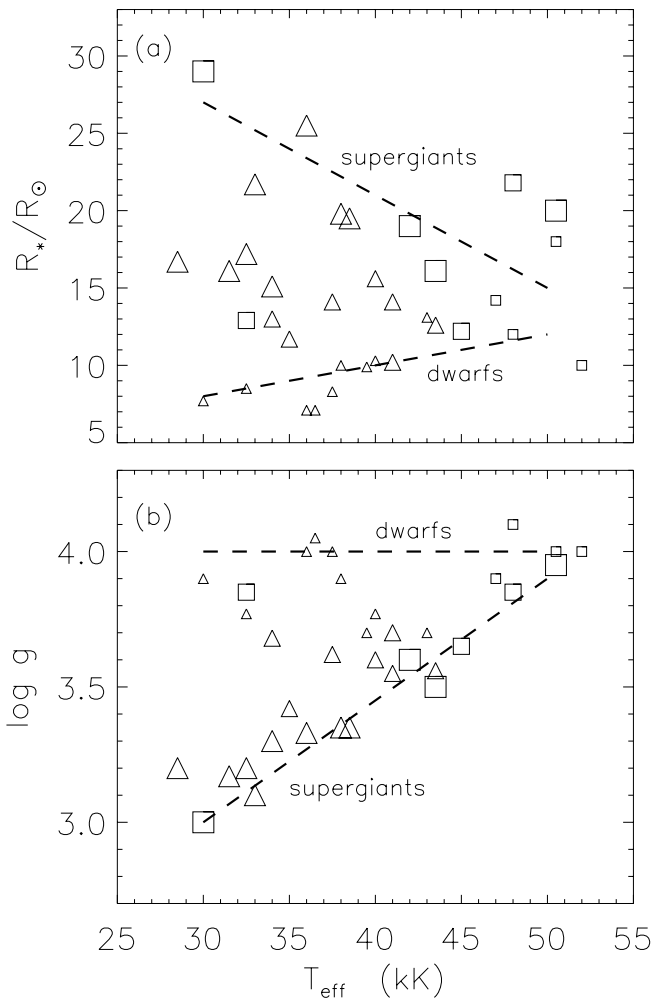

FIG. 1.—Empirical stellar data, (*a*) stellar radii and (*b*) surface gravities, based on data compiled by Herrero et al. 1992 (*triangles*) and Puls et al. 1996 (*squares*). Small, medium, and large symbols represent dwarf, giant, and supergiant stars.

We choose parameter values based on observations. Herrero et al. (1992) and Puls et al. (1996) have determined the surface gravities, effective temperatures, and stellar radii, for samples of OB stars, via the "spectral fitting" method. In these studies, log g and $T_{\rm eff}$ were inferred for individual stars by matching spherical NLTE (but nonblanketed) atmosphere models to the observed hydrogen and helium absorption line profiles in the stellar spectra. Given the best fitting SEDs and predicted surface radiation flux densities, the radii were then inferred given the observed stellar (V-band) luminosities, following the technique introduced by Kudritzki (1980).

In Figure 1, we display log g versus $T_{\rm eff}$, and R_* versus $T_{\rm eff}$, for the samples of OB stars analyzed by Herrero et al. (1992) and Puls et al. (1996). It is evident that the OB stars of various types occupy well defined regions in these diagrams. The empirical data allow us to define relations for

[1] Defined as the radius at which the Rosseland optical depth equals 2/3.

" generic " dwarfs and supergiants. For dwarfs we set

$$\log g = 4 \,, \tag{1}$$

$$\frac{R}{R_\odot} = 0.2 T_{\rm eff} + 2 \tag{2}$$

and for supergiants,

$$\log g = 0.045 T_{\rm eff} + 1.65 \,, \tag{3}$$

$$\frac{R}{R_\odot} = -0.6 T_{\rm eff} + 45 \,. \tag{4}$$

These relations define the approximate boundaries, in these diagrams, within which OB stars of all luminosity classes are known to exist.

Our model atmosphere grid covers the full range of parameters within the triangular wedge that is defined by the dwarf and supergiant sequences in the log g versus $T_{\rm eff}$ diagram (see Fig. 1*a*). We computed atmospheres for $T_{\rm eff}$ ranging from 25 to 55 kK in steps of 1 kK and surface gravities (in cm s^{-2}) ranging from (as low as) 3 to 4 in steps of 0.2 dex. For each $T_{\rm eff}$ and log g pair, we set the stellar radius via linear interpolation, using log g as the independent parameter, and the dwarf and supergiant radii as specified by equations (1)–(4). The surface gravities, stellar radii, and effective temperatures of our models are displayed in Figures 2*a* and 2*b*. The associated *spectroscopic* masses

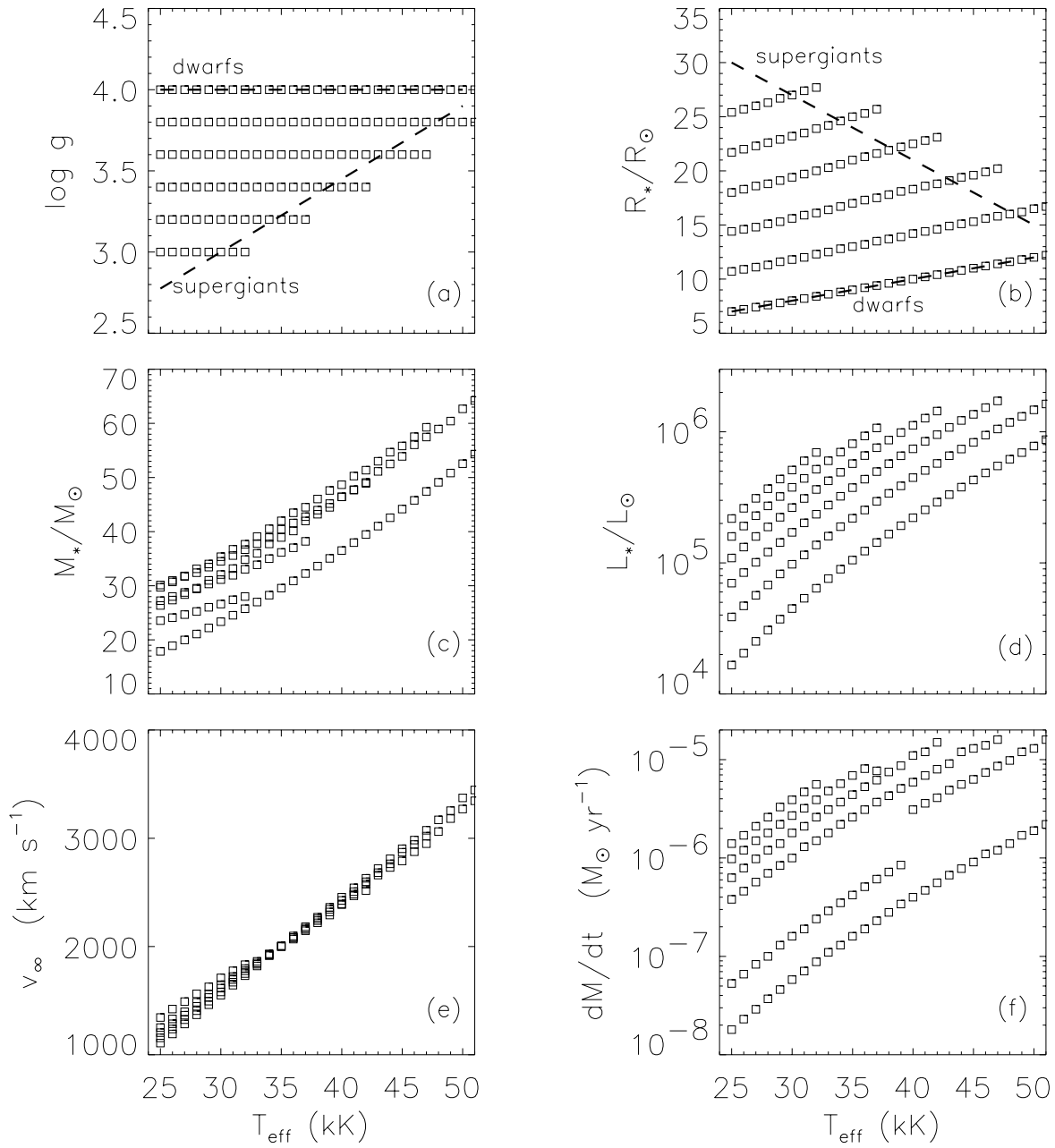

FIG. 2.—Input stellar parameters for the model grid: (*a*) surface gravity log g, (*b*) radius $R/R_\odot$, (*c*) spectroscopic mass $M_*/M_\odot$, (*d*) luminosity $L_*/L_\odot$, (*e*) terminal wind velocity v_∞ (in km s^{-1}), and (*f*) wind mass-loss rate $\dot{M}$ (in $M_\odot$ yr^{-1}). The dashed lines in (*a*) and (*b*) are the dwarf and supergiant sequences as defined by eqs. (1)–(4).

$M_* \equiv gR_*^2/G$ and bolometric luminosities $L_* \equiv 4\pi R_*^2 \sigma T_{\rm eff}^4$ for our models are shown in Figures 2*c* and 2*d*.

The terminal wind velocities, v_∞, of OB stars are directly observable quantities (e.g., Prinja, Barlow, & Howarth 1990; Kudritzki & Puls 2000). Given the terminal velocities, the mass-loss rates, $\dot{M}$, may be determined via the observed wind-momentum-luminosity (WML) relation between the stellar luminosity and the "modified wind momentum" $D_{\rm mom} \equiv \dot{M} v_\infty (R_*/R_\odot)^{0.5}$. The theory of radiatively driven winds predicts that $D_{\rm mom}$ is a simple function of L_*. The empirical WML relation depends on both luminosity class and spectral type, with scatter. We use the expressions assembled and summarized by Kudritzki & Puls (2000). Figure 2*e* shows the resulting empirically based values of v_∞ versus $T_{\rm eff}$ for our low- to high-gravity systems. We adopt an O-star dwarf/giant WML relation for stars with $R_* < 15\ R_\odot$ and a supergiant WML relation for stars for $R_* > 15\ R_\odot$.[2] The resulting mass-loss rates are shown in Figure 2*f*. We have verified that the nonphysical discontinuity in $\dot{M}$ in the $\log g = 3.8$ sequence (see Fig. 2*f*) that is introduced by our WML *Ansatz* does not lead to significant discontinuities in the properties of the model atmospheres.

4. INDIVIDUAL STARS

In Figure 3 we display a subset of our computed stellar atmosphere spectra as functions of $T_{\rm eff}$ and $\log g$, spanning the dwarf to supergiant parameter space. Our full grid of models is available on the World Wide Web.[3] For each model we plot the surface flux density, f_ν, (in ergs s^{-1} cm^{-2} Hz^{-1}) versus the photon energy E from 0 to 5 ryd. For comparison, for each model we also plot the blackbody flux densities, $\pi B_\nu(T_{\rm eff})$, where B_ν is the Planck function.

The stellar SEDs consist of continua with numerous superposed absorption and emission features. Several noteworthy properties are apparent in the model atmosphere flux distributions. First, the enhanced ionizing continua that are expected in extended and expanding atmospheres (Gabler et al. 1989) are moderated and reduced by line-blocking effects (Pauldrach et al. 2001). Second, the prominent Lyman and He I ionization edges at 1 and 1.8 ryd disappear as the effective temperature increases or as the surface gravity is reduced. Third, at high $T_{\rm eff}$ and low $\log g$, the SED continua near the ionization edges approach the blackbody curves.

This behavior can be understood as follows. Because the continuum on each side of an ionization edge is formed at a depth and temperature where the radiation becomes optically thick, and because of the generally larger opacity on the "blue" sides, prominent edges appear in systems with steep temperature gradients. The temperature gradients are, in turn, determined by the associated hydrodynamic density gradients. Thus, when radiation pressure is most effective, as in high-$T_{\rm eff}$ or low–$\log g$ systems, the atmospheres are extended, the density gradients are diminished, and the ionization edges disappear. When this happens, the continuum at all wavelengths becomes optically thick at about the same spatial locations and temperatures. The overall continuum must then approach the blackbody form, given the definition of $T_{\rm eff}$ and flux conservation.

Figure 3 also shows that a He II continuum ($E > 4$ ryd) is absent in low-$T_{\rm eff}$ and low–$\log g$ systems (optically thick winds) but appears at high $T_{\rm eff}$ and high $\log g$ (optically thin winds). This illustrates the well-known fact that in stellar winds the He II continuum makes a sudden transition from optically thick to thin behavior at critical values of the mean wind density, depending on $T_{\rm eff}$ and the electron temperature at the base of the wind (Pauldrach et al. 1990). The transition from thick to thin winds is also triggered by an increase in the surface gravity. The transitions are sudden because near the critical points an increased He II opacity leads to diminished metals ionization and increased line blocking in the He II continuum, leading to a "runaway" increase in the He II opacity.[4]

For each model in our grid we have computed the Lyc and He I flux integrals (in s^{-1} cm^{-2})

$$q_{\rm x} = \int_{\nu_{\rm x}}^{\infty} \frac{f_\nu}{h\nu} d\nu\ , \qquad (5)$$

where $\nu_{\rm x}$ is the ionization frequency for H or He. In Figures 4*a* and 4*b* we plot $q_{\rm H}$ and $q_{\rm He}$ as functions of $T_{\rm eff}$ for the different $\log g$ sequences, and for comparison we also plot the blackbody fluxes. It is apparent that at low $T_{\rm eff}$, both $q_{\rm H}$ and $q_{\rm He}$ are suppressed below the blackbody values. For fixed $T_{\rm eff}$, the fluxes increase and approach the blackbody curves as $\log g$ decreases and the ionization edges weaken and disappear. At high $T_{\rm eff}$, the Lyc and He I fluxes approach the blackbody limits.

In Figures 4*c* and 4*d* we plot the Lyc and He I photon emission rates (in photons s^{-1}), $Q_{\rm H} \equiv 4\pi R_*^2 q_{\rm H}$ and $Q_{\rm He} \equiv 4\pi R_*^2 q_{\rm He}$, as functions of $T_{\rm eff}$ for the various $\log g$ sequences, where the stellar radii R_* are as specified in § 2. In Figures 4*c* and 4*d* we indicate the locations of dwarf and supergiant stars as defined by equations (1)–(4). The photon emission rates are larger for the supergiants because of their larger surface areas and smaller surface gravities. For $T_{\rm eff}$ from 25 to 50 kK, $Q_{\rm H}$ ranges from 1×10^{46} to 5×10^{49} photons s^{-1} for dwarfs, and from 4×10^{47} to 8×10^{49} photons s^{-1} for supergiants. For this temperature range, $Q_{\rm He}$ ranges from 2×10^{43} to 1×10^{49} photons s^{-1} for dwarfs, and from 1×10^{45} to 2×10^{49} photons s^{-1} for supergiants.

Earlier calculations of the Lyc and He I emission rates for hot stars are in overall good agreement with our more sophisticated models, but some important differences do exist, which we now discuss. Specifically, we compare our Lyc and He I flux computations to those presented by Vacca, Garmany, & Shull (1996), Schaerer & de Koter (1997), and Lanz & Hubeny (2003). Vacca et al. based their computations on static plane-parallel LTE models (Kurucz 1992). Schaerer & de Koter carried out computations using their spherical wind *CoStar* models, in which only hydrogen and helium (but not the metals) are treated in NLTE, and in which the temperature structures are derived using an approximate treatment of line blanketing in grey atmospheres. Lanz & Hubeny (2003) used models that do

[2] Following Kudritzki & Puls 2000, we write $\log D_{\rm mom} = \log D_0 + x \log(L/L_\odot)$ and set $\log D_0 = 19.87$ and $x = 1.57$ for $R < 15\ R_\odot$, and $\log D_0 = 20.69$ and $x = 1.51$ for $R > 15\ R_\odot$.

[3] From ftp://wise3.tau.ac.il/pub/stars.

[4] The transition to optically thick winds can also give rise to enhanced radiative acceleration and a corresponding jump in the mass-loss rate, possibly leading to bistable wind behavior (Pauldrach & Puls 1990).

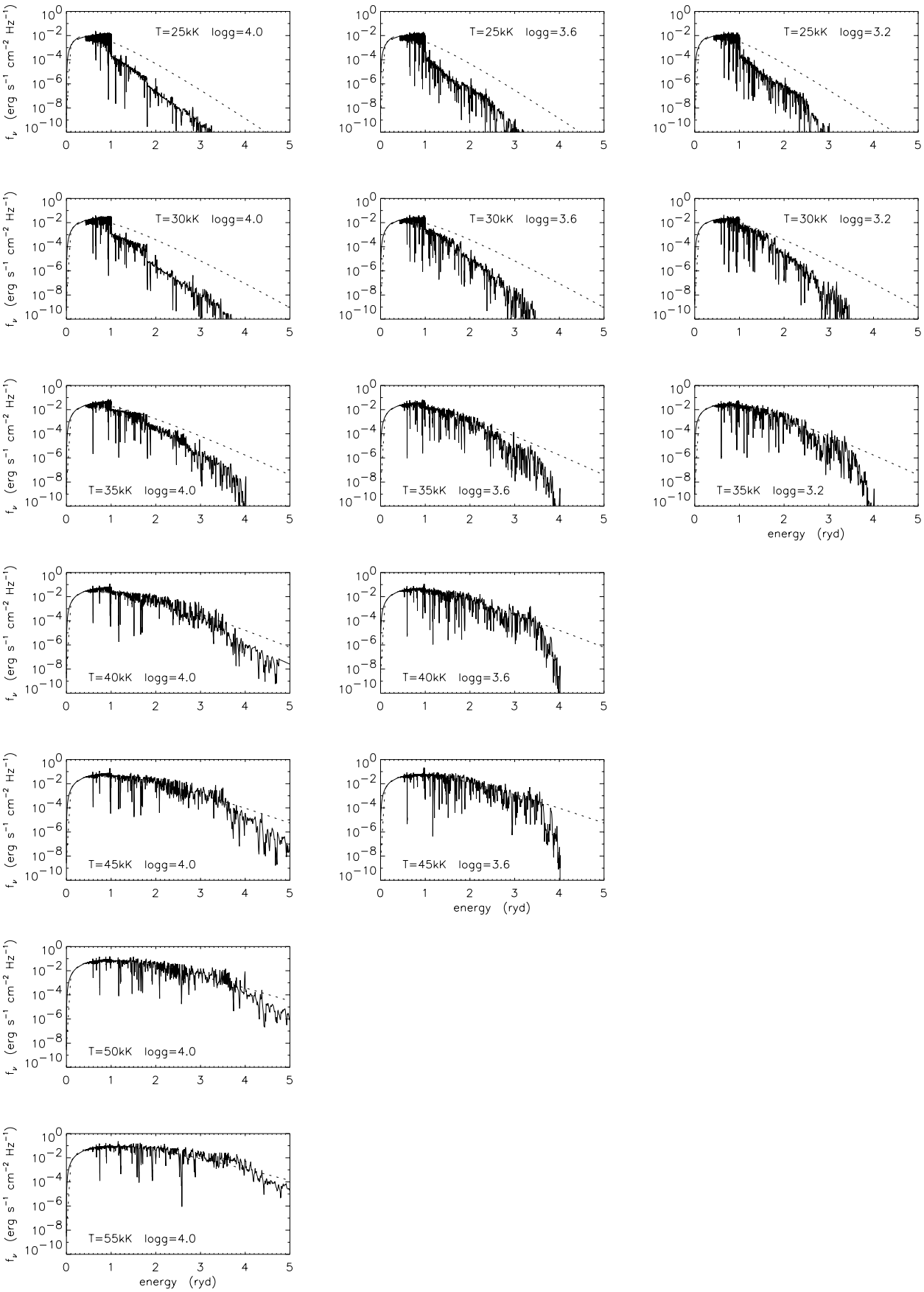

FIG. 3.—Subsample of our model atmosphere grid, with $T_{\rm eff}$ ranging from 25 to 55 kK in steps of 5 kK (*vertical*), and log g ranging from 3.2 to 4 (cm s^{-2}) in steps of 0.4 dex (*horizontal*).

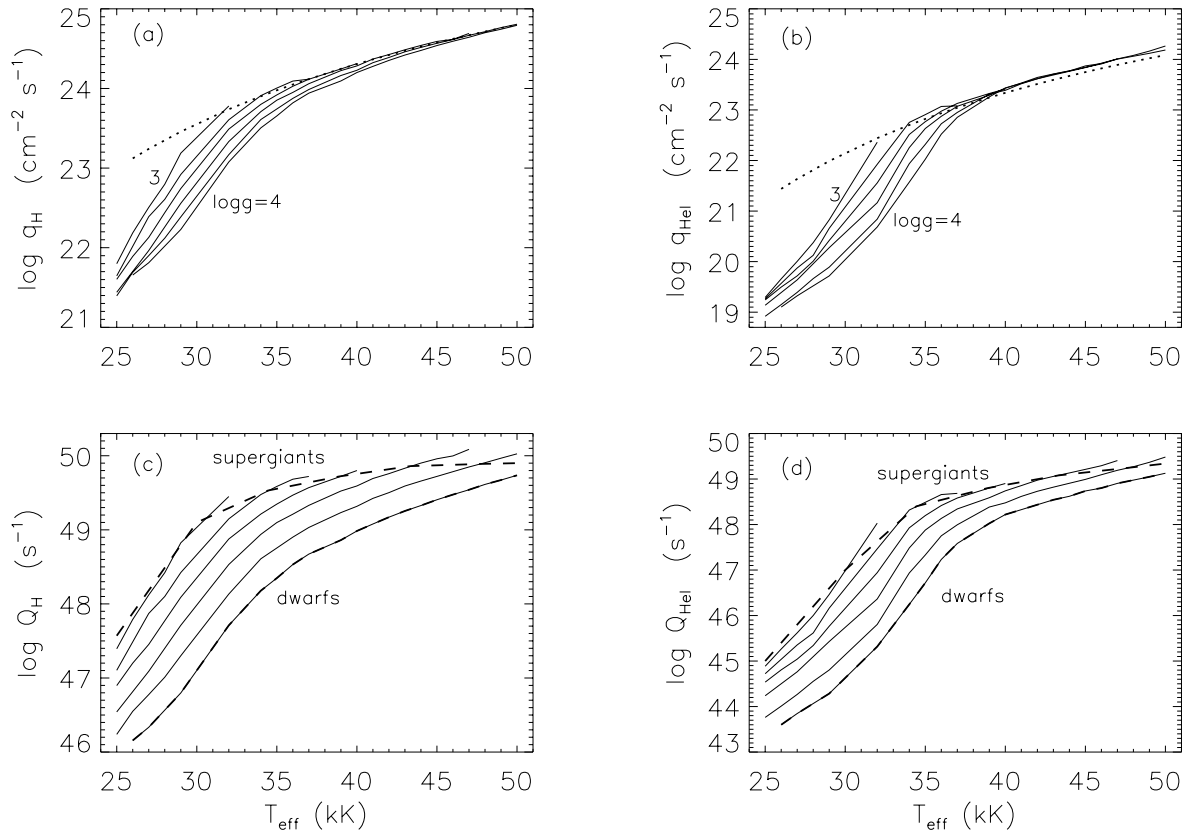

FIG. 4.—(*a*) Lyman continuum surface photon flux q_H (in cm^{-2} s^{-1}), (*b*) He I photon flux q_{He} (in cm^{-2} s^{-1}), (*c*) Lyman continuum photon emission rate Q_H (in s^{-1}), and (*d*) He I photon emission rate Q_{He} (in s^{-1}). The dotted lines in (*a*) and (*b*) are blackbody fluxes $\pi B_\nu(T_{eff})$. The solid curves are for stars with log g ranging from 3 to 4 in steps of $\Delta \log g = 0.2$. The dashed curves in (*c*) and (*d*) are the dwarf and supergiant sequences.

incorporate metals in NLTE, but which are static and plane-parallel.

Lanz & Hubeny (2003) provide computations of q_H and q_{He} for a range metallicities. For solar-metallicity stars, their results are in good agreement with ours at high effective temperatures where the fluxes approach the blackbody curves. However, for $T \lesssim 40$ kK we find lower Lyc and He I fluxes, with the differences increasing to $\sim$0.5 dex, in both q_H and q_{He}, at temperatures below 30 kK.

For purposes of comparison we have constructed models for the identical stellar parameters, T_{eff}, log g, and R_*, that were selected by Vacca et al. (1996), and also adopted by Schaerer & de Koter (1997), for stellar luminosity classes V, III, and I. In Tables 1, 2, and 3, we list these stellar input parameters together with appropriate values for v_∞ and $\dot{M}$ following the procedures described in § 2. We also list the spectral type versus effective temperature calibrations derived by Vacca et al.[5]

In Tables 1–3 we list our results for q_H, q_{He}, Q_H, and Q_{He}, for the specified stellar parameters. We compare our results to the Vacca et al. (1996) and Schaerer & de Koter (1997) computations in Figure 5. The various computations for the Lyc emission rates agree very well at high T_{eff} where the fluxes approach blackbody values. Differences of up to 0.1 dex are present at low T_{eff}, with our values falling midway between the higher Vacca et al. and lower Schaerer & de Koter results for the giants (III) and supergiants (I). Larger differences are present in the He I emission rates. For low T_{eff} our results deviate for the Vacca et al. values by up to $\pm$0.3 dex. At high T_{eff} our results are about 0.3 dex smaller than Schaerer & de Koter, for all luminosity classes. We attribute this difference to our nonrestrictive treatment of NLTE metal line blocking and blanketing in the hydrodynamics, energy balance, and radiative transfer.

[5] More recent calibrations for dwarf stars based on NLTE wind atmospheres (Martins, Schaerer, & Hillier 2002) lower the temperatures for a given spectral class by a few 10^3 K.

5. CLUSTERS

We have incorporated our model atmospheres into our population synthesis code STARS (Sternberg 1998; Thornley et al. 2000) to compute the time-dependent ionizing spectral energy distributions and Lyc and He I photon emission rates for evolving stellar clusters. Our cluster synthesis computations may be used together with observations of stellar continua and nebular hydrogen and helium recombination line data to infer star formation rates and histories in Galactic and extragalactic star-forming regions.

We use the Geneva stellar evolutionary tracks for nonrotating stars with solar metallicity and enhanced mass-loss rates (Schaller et al. 1992; Meynet et al. 1994; Maeder & Meynet 2000) to follow the stellar population distributions

TABLE 1

PARAMETERS FOR OB STARS OF LUMINOSITY CLASS V

Spectral Type	$T_{\rm eff}$ (K)	$\log g$ (cm s^{-2})	R_* ($R_\odot$)	$\log L$ ($L_\odot$)	M ($M_\odot$)	v_∞ (km s^{-1})	$\dot{M}$ ($M_\odot$ yr^{-1})	$\log Q_{\rm H}$ (s^{-1})	$\log Q_{\rm He}$ (s^{-1})	$\log q_{\rm H}$ (cm^{-2} s^{-1})	$\log q_{\rm He}$ (cm^{-2} s^{-1})
O3	51,230	4.149	13.2	6.04	87.6	3552	2.7E−6	49.87	49.29	24.84	24.26
O4	48,670	4.106	12.3	5.88	68.9	3266	1.8E−6	49.68	49.06	24.72	24.09
O4.5	47,400	4.093	11.8	5.81	62.3	3138	1.4E−6	49.59	48.94	24.66	24.01
O5	46,120	4.081	11.4	5.73	56.6	3026	1.1E−6	49.49	48.83	24.59	23.93
O5.5	44,840	4.060	11.0	5.65	50.4	2903	8.9E−7	49.39	48.70	24.52	23.83
O6	43,560	4.042	10.7	5.57	45.2	2784	7.2E−7	49.29	48.56	24.45	23.72
O6.5	42,280	4.030	10.3	5.49	41.0	2666	5.6E−7	49.18	48.46	24.37	23.65
O7	41,010	4.021	10.0	5.40	37.7	2543	4.5E−7	49.06	48.32	24.28	23.53
O7.5	39,730	4.006	9.6	5.32	34.1	2428	3.5E−7	48.92	48.11	24.17	23.36
O8	38,450	3.989	9.3	5.24	30.8	2313	2.7E−7	48.75	47.86	24.03	23.14
O8.5	37,170	3.974	9.0	5.15	28.0	2194	2.1E−7	48.61	47.55	23.92	22.85
O9	35,900	3.959	8.8	5.06	25.4	2083	1.7E−7	48.47	47.17	23.80	22.50
O9.5	34,620	3.947	8.5	4.97	23.3	1972	1.3E−7	48.26	46.63	23.62	21.99
B0	33,340	3.932	8.3	4.88	21.2	1853	1.0E−7	48.02	45.82	23.40	21.20
B0.5	32,060	3.914	8.0	4.79	19.3	1747	7.8E−8	47.71	45.36	23.12	20.77

NOTES.—Effective temperatures, gravities, radii, and spectral classes, are as specified by Vacca et al. 1996. The listed ionizing fluxes were calculated using our model atmospheres.

TABLE 2

PARAMETERS FOR OB STARS OF LUMINOSITY CLASS III

Spectral Type	$T_{\rm eff}$ (K)	$\log g$ (cm s^{-2})	R_* ($R_\odot$)	$\log L$ ($L_\odot$)	M ($M_\odot$)	v_∞ (km s^{-1})	$\dot{M}$ ($M_\odot$ yr^{-1})	$\log Q_{\rm H}$ (s^{-1})	$\log Q_{\rm He}$ (s^{-1})	$\log q_{\rm H}$ (cm^{-2} s^{-1})	$\log q_{\rm He}$ (cm^{-2} s^{-1})
O3	50,960	4.084	15.3	6.15	101.4	3497	1.1E−5	49.98	49.42	24.83	24.27
O4	48,180	4.005	15.1	6.05	82.8	3186	8.4E−6	49.86	49.23	24.71	24.08
O4.5	46,800	3.971	15.0	5.99	75.8	3051	7.3E−6	49.78	49.11	24.64	23.97
O5	45,410	3.931	15.0	5.93	68.4	2912	6.3E−6	49.72	49.01	24.58	23.88
O5.5	44,020	3.891	14.9	5.88	62.0	2782	5.4E−6	49.64	48.90	24.51	23.77
O6	42,640	3.855	14.8	5.82	56.6	2662	4.6E−6	49.56	48.81	24.43	23.69
O6.5	41,250	3.820	14.8	5.76	52.0	2535	3.9E−6	49.46	48.64	24.33	23.52
O7	39,860	3.782	14.7	5.70	47.4	2416	3.3E−6	49.36	48.50	24.24	23.38
O8	37,090	3.700	14.7	5.57	39.0	2170	2.4E−6	49.12	48.09	24.00	22.98
O8.5	35,700	3.660	14.7	5.50	35.6	2062	2.0E−6	49.01	47.87	23.89	22.75
O9	34,320	3.621	14.7	5.43	32.6	1952	1.7E−6	48.86	47.47	23.74	22.35
O9.5	32,930	3.582	14.7	5.36	29.9	1843	1.4E−6	48.67	46.81	23.55	21.69
B0	31,540	3.542	14.7	5.29	27.4	1746	1.1E−6	48.39	46.24	23.27	21.12
B0.5	30,160	3.500	14.8	5.21	25.1	1642	9.2E−7	48.06	45.66	22.93	20.54

TABLE 3

PARAMETERS FOR OB STARS OF LUMINOSITY CLASS I

Spectral Type	$T_{\rm eff}$ (K)	$\log g$ (cm s^{-2})	R_* ($R_\odot$)	$\log L$ ($L_\odot$)	M ($M_\odot$)	v_∞ (km s^{-1})	$\dot{M}$ ($M_\odot$ yr^{-1})	$\log Q_{\rm H}$ (s^{-1})	$\log Q_{\rm He}$ (s^{-1})	$\log q_{\rm H}$ (cm^{-2} s^{-1})	$\log q_{\rm He}$ (cm^{-2} s^{-1})
O3	50,680	4.013	17.8	6.27	115.9	3435	1.6E−5	50.10	49.53	24.82	24.25
O4	47,690	3.928	18.6	6.21	104.7	3119	1.4E−5	50.02	49.34	24.70	24.02
O4.5	46,200	3.866	19.1	6.18	95.7	2973	1.3E−4	49.98	49.29	24.63	23.94
O5	44,700	3.800	19.6	6.14	86.5	2897	1.2E−5	49.93	49.17	24.56	23.80
O5.5	43,210	3.740	20.1	6.10	79.5	2670	1.1E−5	49.87	49.06	24.48	23.67
O6	41,710	3.690	20.6	6.07	74.7	2554	9.6E−6	49.82	48.98	24.41	23.57
O6.5	40,210	3.636	21.2	6.03	69.6	2424	8.7E−6	49.75	48.86	24.31	23.42
O7.5	37,220	3.516	22.4	5.94	59.2	2172	7.0E−6	49.57	48.56	24.08	23.08
O8	35,730	3.456	23.1	5.90	54.8	2057	6.3E−6	49.50	48.42	23.99	22.91
O8.5	34,230	3.395	23.8	5.85	50.6	1948	5.5E−6	49.37	48.14	23.84	22.60
O9	32,740	3.333	24.6	5.80	46.7	1847	4.8E−6	49.24	47.73	23.68	22.17
O9.5	31,240	3.269	25.4	5.74	43.1	1759	4.1E−6	49.04	46.94	23.44	21.35

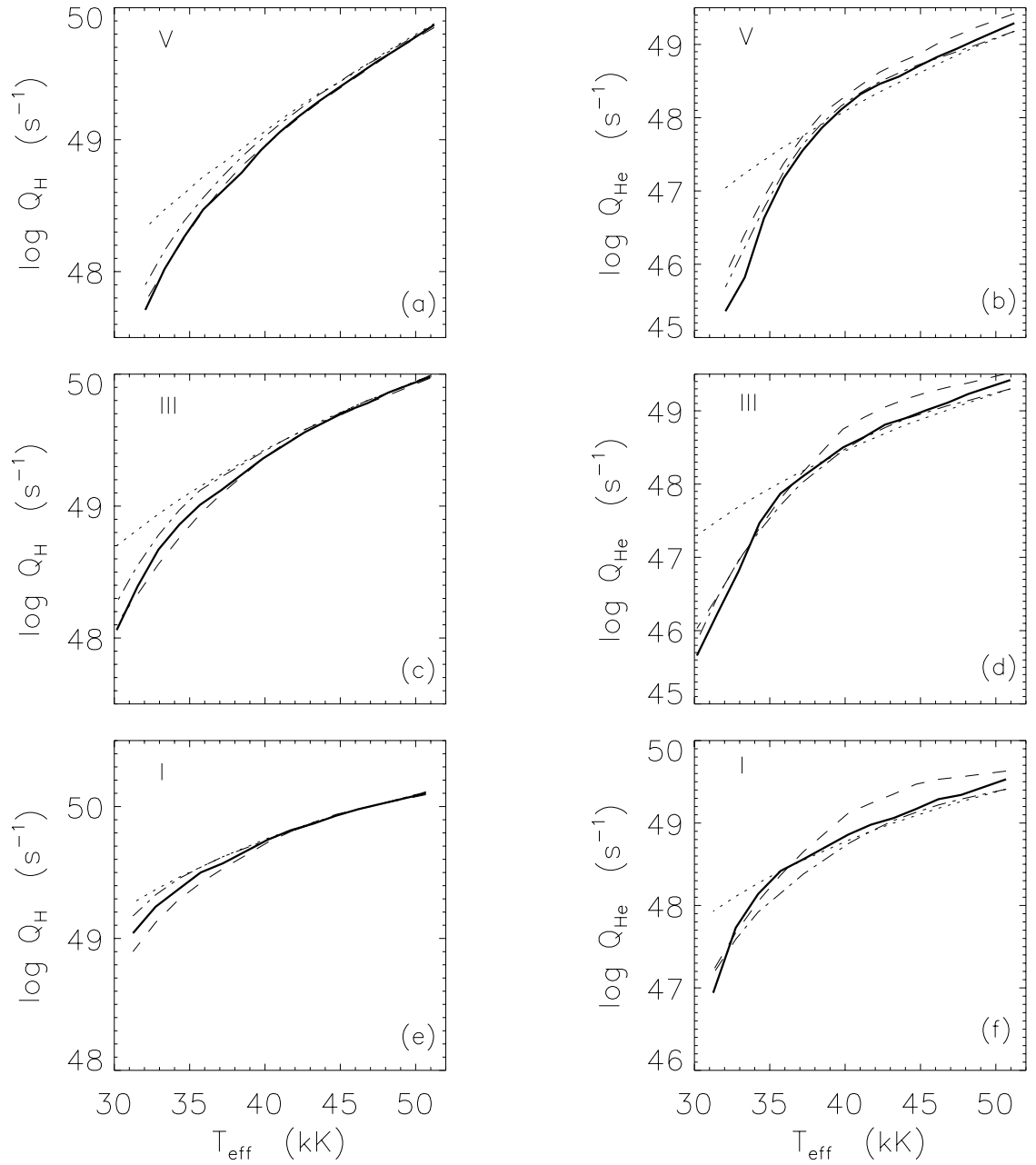

FIG. 5.—Lyman and He I emission rate comparisons, for dwarfs (*a* and *b*), giants (*c* and *d*), and supergiants (*e* and *f*). Values computed in this paper are indicated by the thick solid curves, dashed-dotted curves are the Vacca et al. 1996 rates, long-dashed curves are the *CoStar* Schaerer & de Koter 1997 rates, and dotted curves are the blackbody rates.

in the Hertzsprung-Russell (H-R) diagram. The cluster luminosity density (in ergs s^{-1} Hz^{-1}) can be written as

$$L_\nu(t) = \int_{m_l}^{m_u} \int_{\rm track} \rho_{T,L,g} \frac{L}{\sigma T_{\rm eff}^4} f_\nu(T_{\rm eff},\ g) ds\, dm\ , \quad (6)$$

where $\rho_{T,L,g}$ is the number density of stars per unit "length" along evolutionary tracks, as specified by the zero-age main-sequence masses, at positions $T_{\rm eff}$ and L_* in the H-R diagram, corresponding to *evolutionary* surface gravities $g = GM_*/R_*^2$, where M_* is the (varying) stellar mass along the tracks (with $L_* = 4\pi R_*^2 \sigma T_{\rm eff}^4$). In equation (6), $f_\nu(T_{\rm eff},\ g)$ is the SED for individual stars with temperatures $T_{\rm eff}$ and surface gravities g. The integrations are carried out along the entire tracks for stellar masses ranging from a lower limit m_l to an upper limit m_u.

In our computations we assume that stars form with a Salpeter initial mass function (IMF), so that the number of stars formed per mass interval per unit time is $n_m(t) = k(t)m^{-\alpha}$, with $\alpha = 2.35$, where t is the age of the stellar cluster. The total star formation rate (in $M_\odot$ yr^{-1}) is then

$$R(t) = k(t) \int_{m_l}^{m_u} m^{1-\alpha} dm\ . \quad (7)$$

We note that $\rho_{T_{\rm eff},L,g} ds = n_m(\tau) dt$, where the retarded time, $\tau \equiv t - t_*$, is the lag between the cluster age and the evolutionary age t_* of a star with temperature $T_{\rm eff}$ and

luminosity, L_*, on a given track. The "speed," $v \equiv ds/dt$, is the rate at which stars move along the tracks in the H-R diagram.

Our focus here is the computation of the ionizing SEDs and resulting total Lyc and He I photon emission rates for evolving clusters. OB stars are the primary sources of such radiation, and for these we use our model atmospheres. However, we have also included the contributions of cooler stars (down to 1 $M_\odot$) in our synthesis computations. Such stars make a negligible contribution to the ionizing fluxes but do eventually dominate the longer wavelength optical and infrared radiation. For cool stars we use the Kurucz (1992) library of plane-parallel LTE atmospheres.

We adopt a simplified treatment for the likely minor (but uncertain) contributions of short-lived hot Wolf-Rayet (W-R) stars (e.g., Schaerer & Vacca 1998) to the cluster ionizing SEDs and total Lyc and He I photon emission rates. Recent atmosphere models (Hillier & Miller 1998; see also Smith, Norris, & Crowther 2002) for W-R stars, which incorporate the important effects of metal line blocking, suggest that He II continuum photons ($E > 4$ ryd) are fully absorbed in the dense W-R winds in both the WC and WN phases. Between 1 and 4 ryd, the continua of the model W-R atmospheres are approximately Planckian with superposed emission and absorption features and with increasing absorption near the He II edge (Hillier & Miller 1998). The expectation that W-R stars are minor contributors to the ionizing photon budget in clusters is supported by observations that show that the presence of such stars do not influence the associated nebular ionization states (Bresolin & Kennicutt 2002; Gonzalez-Delgado et al. 2002). Given the uncertainties in the theoretical W-R spectra, we treat the W-R stars as simple blackbodies between 1 and 4 ryd and assume that they emit no photons beyond the He II limit.

In our numerical integration of equation (6) we first interpolated a dense set of 641 tracks from the original set provided by Schaller et al. (1993). The interpolated values of $\log L_*$ and $\log T_{\rm eff}$ were evaluated between equivalent evolutionary stages along adjacent tracks. For a given L_* and $T_{\rm eff}$ along a track, we used the associated (evolutionary) surface gravity to select the nearest appropriate atmosphere from our model grid. The stellar flux densities were then rescaled by the factor $L_*/\sigma T_{\rm eff}^4$ (see eq. [6]) to ensure consistency with the evolutionary luminosities. In our calculations a "mass discrepancy" (e.g., Groenewegen et al. 1989; Herrero et al. 1992) of up to a factor of $\sim$2 exists between the spectroscopic masses as defined in § 3 (see also Fig. 2*c*), and the masses as specified by the evolutionary computations. Corresponding differences of up to 0.2 dex are thus present between the "spectroscopic" and "evolutionary" surface gravities for given values of L_* and $T_{\rm eff}$. We do not attempt to resolve this small inconsistency.

In Figure 6 we plot the evolving cluster luminosity densities, for continuous and impulsive star formation,

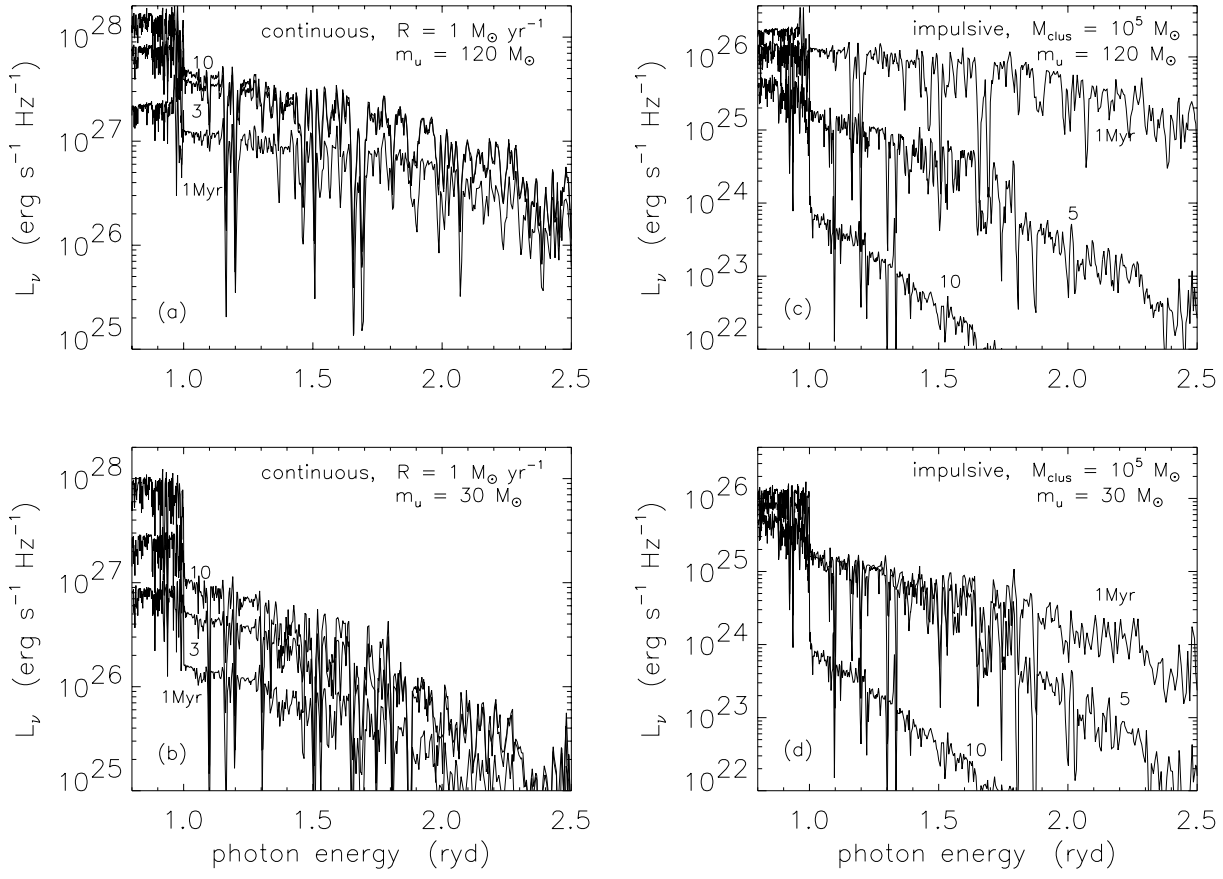

FIG. 6.—Cluster spectral evolution. (*a*) Continuous star formation with $R = 1\ M_\odot\ {\rm yr}^{-1}$, $m_u = 120\ M_\odot$, and cluster ages equal to 1, 3, and 10 Myr. (*b*) Continuous star formation with $R = 1\ M_\odot\ {\rm yr}^{-1}$, $m_u = 30\ M_\odot$, and cluster ages equal to 1, 3, and 10 Myr. (*c*) Impulsive star formation with cluster mass $M_{\rm clus} = 10^5\ M_\odot$, $m_u = 120\ M_\odot$, and cluster ages equal to 1, 5, and 10 Myr. (*d*) Impulsive star formation with cluster mass $M_{\rm clus} = 10^5\ M_\odot$, $m_u = 30\ M_\odot$, and cluster ages equal to 1, 5, and 10 Myr.

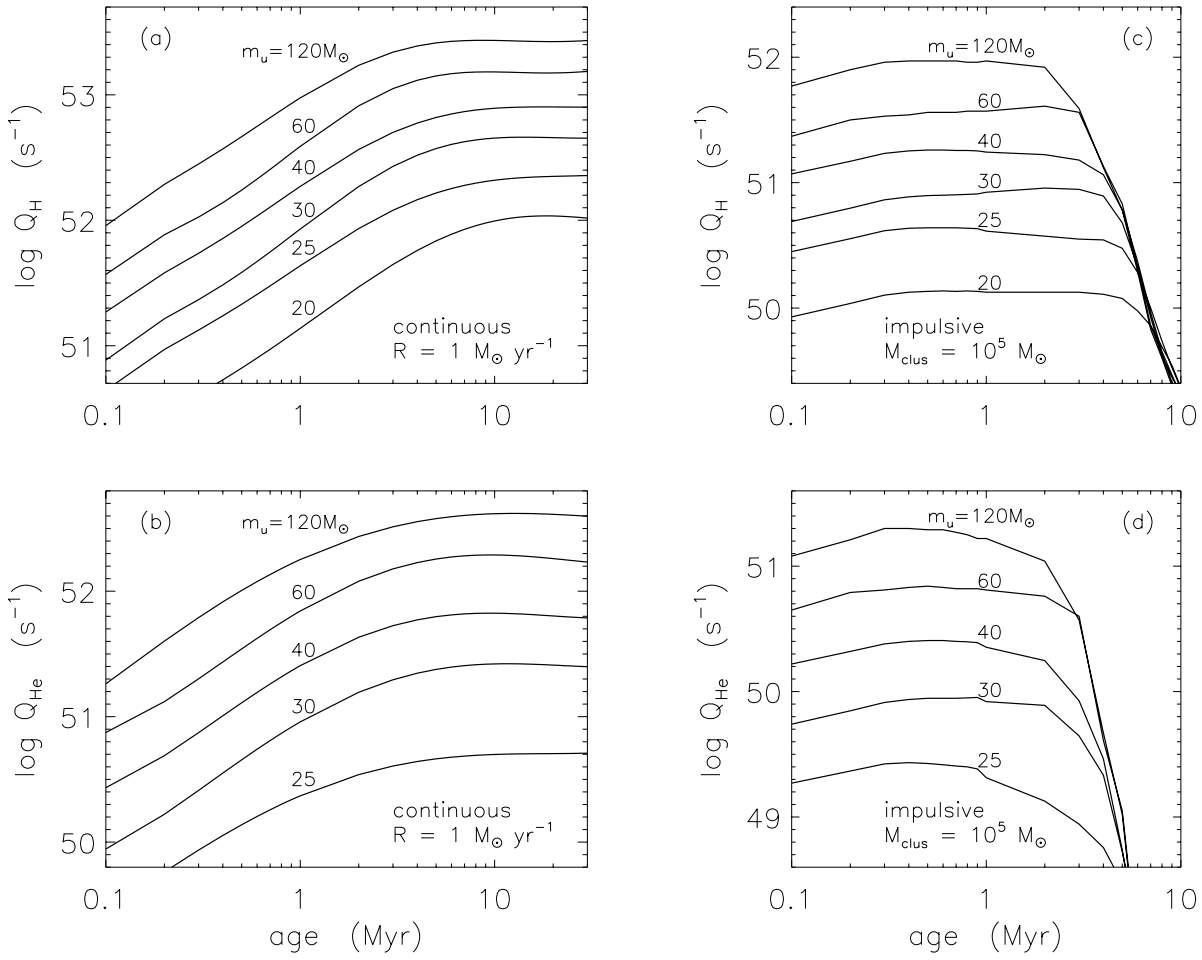

FIG. 7.—(*a*) Cluster Lyman continuum photon emission rate Q_H (s^{-1}) and (*b*) He I emission rate Q_{He}, for continuous star formation with $R = 1\ M_\odot\ yr^{-1}$. (*c*) Lyman emission rate Q_H and (*d*) He I emission rate Q_{He}, for impulsive star formation for a cluster mass $M_{clus} = 10^5\ M_\odot$. In these computations a Salpeter IMF is assumed with an upper mass cutoff m_u ranging from 25 to 120 $M_\odot$.

assuming Salpeter IMFs with a lower (evolutionary) mass limit of $m_l = 1\ M_\odot$, and upper-mass limits m_u equal to 30 and 120 $M_\odot$. We display the behavior of the SEDs from 0.8 to 2.5 ryd. Higher energy photons contribute negligibly to the total Lyc and He I emission rates.

For the continuous models we assume a constant star formation rate $R = 1\ M_\odot\ yr^{-1}$ between m_l and m_u. For these models, the luminosity densities initially increase with cluster age as the numbers of hot stars grow. The ionizing continua approach equilibrium at ~10 Myr as the total numbers of OB stars in the clusters reach equilibrium. The SEDs steepen slightly, and the magnitudes of the Lyman edges correspondingly increase, as the relative numbers of late versus early type O stars increase and approach equilibrium.

For the impulsive models, we assume that a cluster with total mass $M_{clus} = 10^5\ M_\odot$ is formed instantaneously. We again assume a Salpeter IMF with $m_l = 1\ M_\odot$ and m_u equal to 30 or 120 $M_\odot$. For the impulsive bursts the cluster luminosity densities decay with time as the most massive and luminous stars disappear from the systems. The SEDs steepen sharply, and the Lyman edges grow, as the clusters age and the hottest stars with the shortest lifetimes disappear.

In Figure 7 we plot the integrated Lyc and He I photon emission rates, Q_H and Q_{He}, for the evolving clusters. We display results for upper mass IMF limits m_u equal to 20, 25, 30, 40, 60, and 120 $M_\odot$. For continuous star formation, the emission rates initially increase linearly with cluster age. Equilibrium is reached after a time corresponding to the lifetimes[6] of the most massive (and dominating) stars in the system. The equilibrium rates are sensitive to the upper mass limit. For example, the asymptotic Lyc emission rates increase by a factor of 25, from 1.0×10^{52} to $2.5 \times 10^{53}\ s^{-1}$ (for $m_l = 1\ M_\odot$ and $R = 1\ M_\odot\ yr^{-1}$), as m_u is increased from 20 to 120 $M_\odot$.

For impulsive bursts, the photon emission rates are approximately constant at early times, increase slightly during the supergiant phases, and then decay rapidly as the hot stars disappear. The maximal emission rates are sensitive to m_u. The peak Lyc emission rates increase by a factor of 80, from 1.2×10^{50} to $1.0 \times 10^{52}\ s^{-1}$ (for $m_l = 1\ M_\odot$ and $M_{clus} = 10^5\ M_\odot$), as m_u is increased from 20 to 120 $M_\odot$.

We thank I. Hubeny and T. Lanz for helpful comments and U. Giveon for his assistance with the WM-*basic* computations. We thank the German-Israeli Foundation for Research and Development (grant I-0551-186.07/97) for supporting our research.

[6] Rotation may increase the stellar lifetimes by up to ~30% (Meynet & Maeder 2000).

REFERENCES

Abbott, D. C. 1982, ApJ, 263, 723
Bresolin, F., & Kennicutt, R. C. 2002, ApJ, 572, 838
Bruzual, G., & Charlot, S. 1993, ApJ, 405, 538
Castor, J. I., Abbott, D. C., & Klein, R. I. 1975, ApJ, 195, 157
Gabler, R., Gabler, A., Kudritzki, R.-P., Pauldrach, A. W. A., & Puls, J. 1989, A&A, 226, 162
Giveon, U., Sternberg, A., Lutz, D., Feuchtgruber, H., & Pauldrach, A. W. A. 2002, ApJ, 566, 880
Gonzalez-Delgado, R. M., Leitherer, C., Stasinska, G., & Heckman, T. M. 2002, ApJ, 580, 824
Grevesse, N., & Sauval, A. J. 1998, Space Sci. Rev., 85, 161
Groenewegen, M. A. T., Lamers, H. J. G. L. M., & Pauldrach, A. W. A. 1989, A&A, 221, 78
Herrero, A., Kudritzki, R. P., Vilchex, J. M., Kunze, D., Butler, K., & Haser, S. 1992, A&A, 261, 209
Hillier, D. J., & Miller, D. L. 1998, ApJ, 496, 407
Kudritzki, R.-P. 1980, A&A, 85, 174
Kudritzki, R.-P., & Puls, J. 2000, ARA&A, 38, 613
Kurucz, R. L. 1992, in IAU Symp. 149, The Stellar Populations of Galaxies, ed. B. Barbuy & A. Renzini (Dordrecht: Kluwer), 225
Lanz, T., & Hubeny, I. 2003, ApJS, 146, 417
Lee, H., Grebel, E., & Hodge, P. W. 2003, A&A, 401, 141
Leitherer, C., & Heckman, T. M. 1995, ApJS, 96, 9
Leitherer, C., et al. 1999, ApJS, 123, 3
Maeder, A., & Meynet, G. 2000, A&A, 361, 159
Maoz, D., Barth, A. J., Ho, L. C., Sternberg, A., & Filippenko, A. V. 2001, AJ, 121, 3048
Martins, F., Schaerer, D., & Hillier, D. J. 2002, A&A, 382, 999
McKee, C. F., & Williams, J. P. 1997, ApJ, 476, 144
Meynet, G., & Maeder, A. 2000, A&A, 361, 101
Meynet, G., Maeder, A., Schaller, G., Schaerer, D., & Charbonnel, C. 1994, AAS, 103, 97
Mihalas, D. 1967, ApJ, 150, 909
Panagia, N. 1973, AJ, 78, 929
Pauldrach, A. W. A., Hoffmann, T. L., & Lennon, M. 2001, A&A, 375, 161
Pauldrach, A. W. A., Kudritzki, R.-P., Puls, J., & Butler, K. 1990, A&A, 228, 125
Pauldrach, A. W. A., & Puls, J. 1990, A&A, 237, 409
Prinja, R. K., Barlow, M. J., & Howarth, I. D. 1990, ApJ, 361, 607
Puls, J. et al. 1996, A&A, 305, 171
Schaerer, D. 2003, A&A, 397, 527
Schaerer, D., & de Koter, A. 1997, A&A, 322, 598
Schaerer, D., & Vacca, W. D. 1998, ApJ, 497, 618
Schaller, G., Schaerer, D., Meynet, G., & Maeder, A. 1992, AAS, 96, 269
Shapley, A. E., Steidel, C. C., Pettini, M., & Adelberger, K. L. 2003, ApJ, 588, 65
Smith, L. J., Norris, R. P. F., & Crowther, P. A. 2002, MNRAS, 337, 1309
Sternberg, A. 1998, ApJ, 506, 721
Thornley, M. D., Forster-Schreiber, N. M., Lutz, D., Genzel, R., Spoon, H. W. W., Kunze, D., & Sternberg, A. 2000, ApJ, 539, 641
Tumlinson, J. & Shull, J. M. 2000, ApJ, 528, L65
Vacca, W. D., Garmany, C. D. & Shull, J. M. 1996, ApJ, 460, 914
Whitmore, B. C., Zhang, Q., Leitherer, C., Fall, S. M., Schweizer, F., & Miller, B. W. 1999, AJ, 118, 1551